

Impact of Carbonization Temperature on the Structure and Li Deposition Behavior of 3D Dual Metal Carbon Fibers

Dana Schmidt, Sandro Schöner, Michael K. Steinhoff, Roland Schierholz, Kevin Steinhauer, Davis Thomas Daniel, Sebastian Speer, Ansgar Kretzschmar, Fabian Jeschull, Anna Windmüller, Chih-Long Tsai, Hermann Tempel, Shicheng Yu,* and Rüdiger-A. Eichel

Li deposition within lithiophilic–lithiophobic metal carbon fibers is influenced by several structural factors, including electrical conductivity, surface-bound functional groups, particle size and distribution of the lithiophilic–lithiophobic components, which are significantly affected by the carbonization temperature. To gain a deeper understanding of how these different parameters affect the Li deposition behavior, a detailed analysis of Ag and Cu containing carbon fibers at carbonization temperatures from 500 to 1000 °C is performed. At lower carbonization temperatures, the fibers exhibit an unordered carbon structure with a high concentration of heteroatoms and a lithiophilic–lithiophobic gradient. However, the high electrical resistance at these temperatures impedes Li-ion interaction with the fibers, leading to the formation of mossy and dead Li. In contrast, higher carbonization temperatures result in the removal of heteroatoms and a more ordered carbon structure. The agglomeration of Cu and Ag particles at these temperatures disrupts the lithiophilic–lithiophobic gradient, causing concentrated Li deposition on top of the fibers. A threshold temperature of 700 °C has been identified for achieving homogeneous Li deposition. At this temperature, the lithiophilic–lithiophobic gradient still exists, and the more ordered carbon structure enhances Li-ion interaction with the fibers, resulting in stable Li deposition for over 1100 h.

Furthermore, 3D carbonaceous materials have the advantage of being low cost and lightweight, especially in comparison with their metallic counterparts.^[2,3] Due to the unique combination of advantages, 3D carbon-based materials have become increasingly attractive for energy storage applications.^[4–7]


As recently shown by several publications, using 3D carbon fibers as current collectors can effectively reduce the local current density due to an increase of the electroactive surface area, inhibiting concentrated Li deposition and thereby suppressing Li dendrite formations.^[8–12] Furthermore, large volumetric changes during Li plating/stripping are intercepted by the 3D structure, thus reducing the stress at the interface of the deposited Li and stabilizing the solid–electrolyte interface (SEI).^[13–15] However, pure porous carbon structures show a lack of Li-ion affinity, hindering a defined Li-ion guidance near the electrode–electrolyte interface.^[16] Using polar functional groups

can improve the Li-ion adsorption properties due to their lithiophilic nature.^[17,18] For instance, polyacrylonitrile (PAN) has become the most common carbon source due to its relatively high carbon yield after conversion, enabling thermal stability and differently oriented carbon fiber microstructures.^[19,20] As demonstrated for pure PAN-based carbon fibers, carbonization

1. Introduction

Porous carbon fibers are considered a 3D structural matrix material with a wide variety of structural and mechanical properties, including adjustable electrical conductivities, different functional groups by heteroatom doping, and high specific surface areas.^[1]

D. Schmidt, S. Schöner, M. K. Steinhoff, R. Schierholz, K. Steinhauer, D. Thomas Daniel, S. Speer, A. Kretzschmar, A. Windmüller, C.-L. Tsai, H. Tempel, S. Yu, R.-A. Eichel
Institute of Energy Technologies–Fundamental Electrochemistry (IET-1)
Forschungszentrum Jülich
52428 Jülich, Germany
E-mail: s.yu@fz-juelich.de

 The ORCID identification number(s) for the author(s) of this article can be found under <https://doi.org/10.1002/ssstr.202400311>.

© 2024 The Author(s). Small Structures published by Wiley-VCH GmbH. This is an open access article under the terms of the Creative Commons Attribution License, which permits use, distribution and reproduction in any medium, provided the original work is properly cited.

DOI: 10.1002/ssstr.202400311

D. Schmidt, S. Schöner, M. K. Steinhoff, S. Speer, R.-A. Eichel
Material and Processes of Electrochemical Energy Storage and Conversion
RWTH Aachen University
52074 Aachen, Germany

F. Jeschull
Institute for Applied Materials–Energy Storage Systems (IAM-ESS)
Karlsruher Institute of Technologie (KIT)
76344 Eggenstein Leopoldshafen, Germany

R.-A. Eichel
Institute of Energy Materials and Devices
Helmholtz Institute Münster: Ionics in Energy Storage (IMD-4/HI MS),
Forschungszentrum Jülich
48149 Münster, Germany

temperatures have a significant effect on atomic structure and Li-ion storage properties.^[21] While at low carbonization temperatures, Li ions can be stored at defect sites and between graphene layers, removing heteroatoms at elevated carbonization temperatures leads to the storage of Li ions only between graphene layers.^[21]

In addition, it has been reported that thin films of lithiophilic elements such as silver (Ag) or magnesium on current collectors can assist in a more homogenous Li deposition.^[22,23] The lithiophilic metals guide the Li ions uniformly to the energetically preferred lithiophilic metal, reducing the nucleation overpotential for metallic Li and enabling a more uniform Li distribution.^[24] However, large volume changes of the thin lithiophilic layers inhibit their use and motivated researchers to combine both strategies, as first shown by Zhang et al. with a lithiophilic–lithiophobic composite 3D interlayer, out of lithiophobic carbon nanotubes and lithiophilic ZnO particles at the bottom of the 3D carbon skeleton.^[25] Using this composite interlayer on top of a Li-metal anode, the Li ions could be precisely guided to the bottom of the interlayer due to the enhanced negative Gibbs formation energy between lithiophilic elements and Li ions.^[25]

Nevertheless, concentration gradients in 3D skeletons face the challenges of sluggish ion diffusion kinetics and prolonged diffusion pathways, leading to preferential top lithium deposition of the carbon skeleton with time.^[26,27] Thus, it potentially accelerates cell failure. Instead, creating a lithiophilic–lithiophobic gradient on each fiber by incorporating two different kinds of metal into each carbon fiber should homogenize the Li deposition and overcome the kinetic competition between lithium-ion transport and interfacial reactions. The evenly distributed lithiophilic metal particle will homogeneously guide the Li-ion flow into the fiber interior.^[28,29] At the same time, the lithiophobic metal prevents Li top-plating within the 3D skeleton due to the high nucleation

energy barrier and enhances the electrical field.^[30,31] However, the number of influencing factors on the Li distribution in this kind of dual metal carbon fibers is also significantly enhanced, including the electronic conductivity, the electrical field distribution, the pore structure, and the size and distribution of the lithiophilic–lithiophobic metal particles, clearly complicating the understanding of Li deposition behavior.^[25] A fundamental understanding of the chemical structure and corresponding electrochemical behavior at different carbonization temperatures is still lacking but essential to tailor the properties of lithiophilic–lithiophobic 3D dual metal carbon fibers as interlayers or current collector modifications for next-generation battery configurations, like Li-metal or zero-excess Li-metal batteries.

Here, a detailed investigation of the structural evolution of 3D lithiophilic (Ag)–lithiophobic (Cu) carbon fibers at different carbonization temperatures and the corresponding correlation between the structural features and Li deposition is conducted. Particular emphasis is placed on understanding how the evolution of carbon structure and the size and distribution of metal particles influence Li deposition behavior at a large carbonization temperature range of 500–1000 °C.

2. Results and Discussion

The preparation of the 3D dual metal carbon fibers is schematically illustrated in Figure 1a and described in detail in the Experimental Section. The porous green fibers, namely, CuAgC_{Elekt}, are received after an electrospinning step, followed by cross-linking and stabilization in the air at 250 °C, leading to CuAgC_{Stab}. Afterward, all fibers are reduced under Ar/H₂ (3 vol.-%) for 2.5 h at 500 °C and finally carbonized under argon (Ar) atmosphere for 3 h at different temperatures ranging from

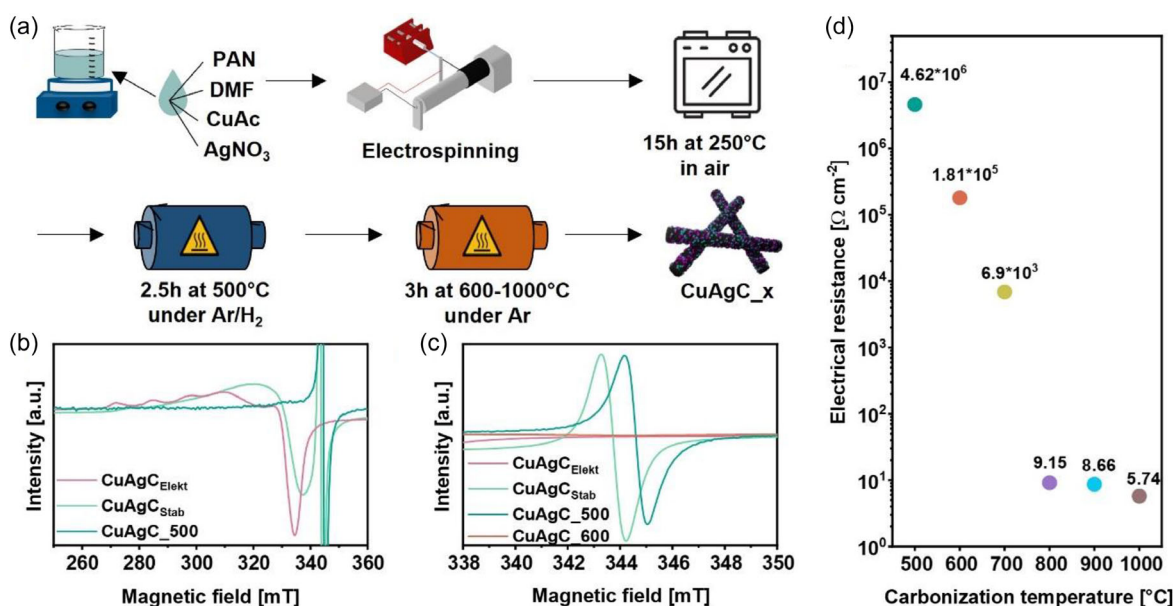


Figure 1. a) Schematic illustration of the synthesis route for CuAgC_x ($x = 500\text{--}1000\text{ °C}$). b) X-Band continuous wave EPR spectra of CuAgC species at 295 K showing the contributions from Cu²⁺ and c) free radicals. All samples treated at carbonization temperatures above 500 °C do not show a contribution from the free radicals, and only CuAgC₆₀₀ was included within the spectrum for clarity in (c). d) The electrical resistance of the samples treated at different carbonization temperatures from 500 to 1000 °C.

600 to 1000 °C. Samples are referred as CuAgC_x to identify the carbonization temperature used, with *x* describing the corresponding temperature.

The preparation of dual metal carbon fibers was investigated using electron paramagnetic resonance (EPR) measurements to gain information about the evolution of the chemical structure after each step in the synthesis. As shown in Figure 1b, CuAgC_{Elekt} and CuAgC_{Stab} exhibit EPR signals characteristic of Cu²⁺ with four hyperfine lines due to the interaction between the unpaired electron spin and the Cu nucleus. In the case of CuAgC_{Elekt}, the EPR signal likely arises from the precursor, copper acetate (CuAc), in its monomeric form. From the EPR spectrum, values of *g*_{||} and *A*_{||} (hyperfine coupling constant) were 2.368 and 12.5 mT, respectively, which agrees with previous reports for monomeric Cu²⁺[H₃COO⁻]₂.^[32,33] The hyperfine structure becomes less resolved in the case of CuAgC_{Stab} and a change in hyperfine coupling is evident from the shift of the low field hyperfine line, indicating a change in the ligands or geometry.^[34] Contribution from CuAc dimers was only present in the case of CuAgC_{Elekt}, indicated by the broad, featureless signals shown in Figure S1, Supporting Information, due to the triplet state transitions in the case of a dimer.^[33] The thermal evaporation of the acetate occurs during the oxidation step at 250 °C in air, releasing gases of CO₂ and acetone with the concomitant formation of copper oxide (CuO).^[35] The successful reduction of CuO to Cu during the reduction step at 500 °C under Ar/H₂ flow is then confirmed by the loss of the Cu²⁺ EPR signal for CuAgC₅₀₀. Along with changes to the CuAc precursor, changes in the carbon structure can be inferred from the EPR spectra by inspecting the changes in the magnetic field region of 338 to 350 mT. Figure 1c shows the presence of free radical signals in this region for CuAgC_{Elekt}, CuAgC_{Stab}, and CuAgC₅₀₀. A contribution from free radicals was not apparent in CuAgC_{Elekt} but is evident in CuAgC_{Stab} and CuAgC₅₀₀ as EPR lines with *g* values (*g* = 1.9987 to 2.0024) and linewidths (0.8–1 mT) typical of free radicals. Upon reduction at 500 °C, the EPR line in the case of CuAgC_{Stab} at *g* = 2.0023 corresponding to free electrons shifts to *g* = 1.9987 for CuAgC₅₀₀, indicating a change in the molecular environment of the radical species. The presence of free-electron radicals in CuAgC_{Stab} is caused by the formation of the ladder structure during the stabilization step under air, with some linear PAN macromolecules in between. A fraction of an ideal ladder unit is visualized in Figure S2, Supporting Information. The ladder structure is obtained by cyclization and dehydrogenation reactions during the degradation of PAN, which also initiates the free-radical transfer process and causes the narrow signal (0.8 mT) for CuAgC_{Stab} in the EPR spectrum. Once the reaction starts, the highly reactive radicals can capture hydrogen atoms in the molecule chains and cause chain reaction characteristic of spontaneity after initiation till termination. Thereby, some oxygen or nitrogen containing functional groups can react with other radicals or can escape from the bulk chains, leading to a chemical structure rearrangement and the loss of some C, N, and O groups in the form of CO₂, CO, N₂, and H₂O. As the temperature reaches 500 °C, free radicals are still present and formed by the spontaneous breakage of linear molecular segments, as shown for CuAgC₅₀₀ in Figure 1c. Further increasing the temperature to 600 °C, the dual metal carbon fibers are mainly formed by aromatized and cross-linked

segments without free radicals, explaining the loss of the free radical EPR signal for carbonization temperatures above 500 °C.^[36] However, the resonator quality factor (*Q*) can still be obtained for carbonization temperatures above 500 °C and can be qualitatively related to the electrical conductivity of the samples.^[37] A decreasing *Q* value is related to increasing conductivity and, as can be seen in Figure S3, Supporting Information, the *Q* value decreases gradually with increasing carbonization temperature. Therefore, the highest electrical conductivity can be assigned to CuAgC₁₀₀₀. However, the largest difference in *Q* value is noticeable between CuAgC₇₀₀ and CuAgC₈₀₀, while CuAgC₉₀₀ and 1000 no longer show any significant change. The same trend can be seen in Figure 1d, where the electrical resistance was measured using the four-point-probe method. A general decrease in the electrical resistance with rising the carbonization temperature is observed, with the most significant change by raising the temperature from 700 to 800 °C (6.9 · 10³ to 9.15 Ω cm⁻²). The reduced electrical resistance is usually related to increased aromatic carbon compounds with delocalized π-electrons in the dual metal carbon fibers.^[38] As the carbonization temperature increases, heteroatoms such as H, N, and O can be removed from the carbon structure, resulting in further cyclization and a higher proportion of aromatics.

To prove the hypothesis, the carbon structure of the prepared dual metal carbon fibers was investigated by Raman measurements. Figure 2a shows the Raman spectra of all samples and the splitting of the two dominant bands (at 1348 cm⁻¹ (D) and 1590 cm⁻¹ (G)) into the five first-order Raman bands D1–D4 and G. The deconvolution of the spectra is based on the methodology proposed by Brubaker et al.^[39] for PAN-containing carbon fibers, which were applied to all six carbonization temperatures. Fitting details can be found in Table S1, Supporting Information. The two visible bands around 1348 and 1590 cm⁻¹ mainly contain the D1 and G band. The D1 band is assigned to a vibrational mode of the disordered graphitic lattice with A_{1G} symmetry, the G band is described by a vibrational mode of the graphitic lattice with E_{2G} symmetry.^[40,41] The D2 band at around 1600 cm⁻¹ is characterized by the same vibrational mode as the G band but originates from disorder-induced phonon mode due to crystal defects.^[42] The first shoulder at 1200 cm⁻¹ is assigned to the D4 band and attributed to a disordered graphite lattice formed by sp²–sp³ bonds at the edges of the carbon rings. The second shoulder at 1500 cm⁻¹ is visualized by the D3 band, originating from interstitial defects in the carbon structure associated with amorphous sp² bonded forms that may include functionalized small molecules.^[43,44]

By comparing the surface area ratios of A_{D1}/A_G and A_{D3}/A_{Sum}, the change in the order of the carbon structure with increasing carbonization temperature can be examined. Figure 2b shows a downward trend for both ratios (A_{D1}/A_G and A_{D3}/A_{Sum}) at rising temperatures. The decreasing proportion of A_{D3}/A_{Sum} indicates the removal of heteroatoms from the carbon fibers at higher carbonization temperatures. The associated increase in the cyclization of the carbon rings is evident by the decreasing area ratio of A_{D1}/A_G, which implies greater structural order in the carbon structure. These findings are further confirmed by the thermogravimetric analysis (TGA) measurement coupled with mass spectroscopy (MS) of CuAgC_{Stab} first

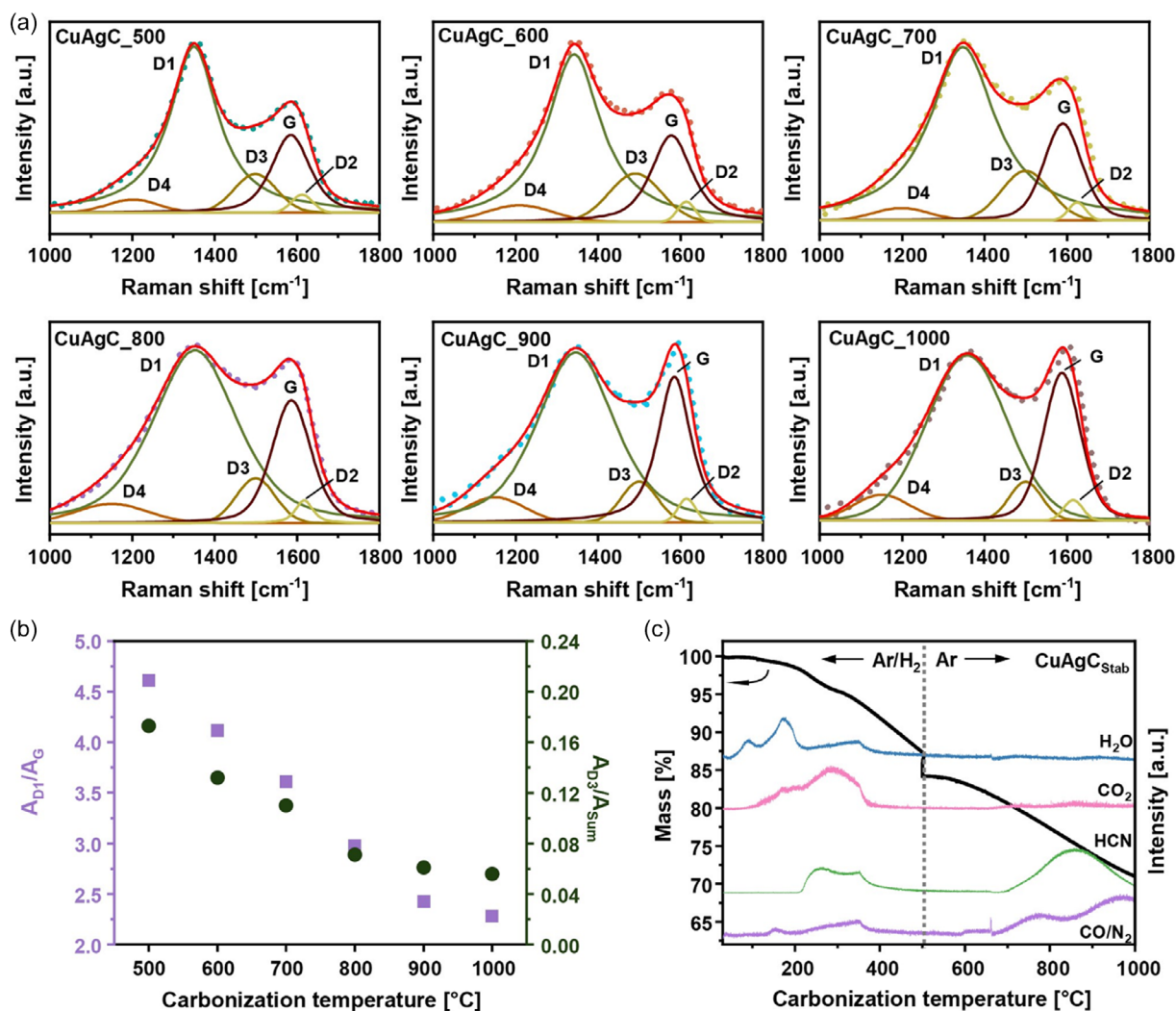


Figure 2. a) Raman spectra of CuAgC_x ($x = 500\text{--}1000$ °C) including the fitting of the first-order Raman bands (G and D1–D4) and in b) a comparison of the different ratios of A_{D1}/A_G and A_{D3}/A_{Sum} for the applied carbonization temperatures from 500 to 1000 °C. The fitting details can be found in Table S1, Supporting Information. c) TGA measurement coupled with MS of CuAgC_{Stab}. The measurement was performed under Ar/H₂ for temperatures up to 500 °C and under pure Ar from 600 to 1000 °C.

under Ar/H₂ (until 500 °C) and followed under an Ar flow from 600 to 1000 °C, as visualized in Figure 2c. The removal of heteroatoms can be divided into three temperature regions, first up to 200 °C, mainly dehydration and the release of –OH groups occur through the formation of H₂O. Afterward, until 500 °C, additional heteroatoms, mainly in the form of CO₂ and small amounts of HCN/CO, are removed from the carbon structure. During the carbonization under Ar from 600 to 1000 °C, further cyclization occurs, causing the release of nitrogen containing groups, such as HCN and N₂.

A deeper understanding of the surface composition and functional groups of CuAgC_x ($x = 500\text{--}1000$ °C) was obtained by X-ray photoelectron spectroscopy (XPS) measurements. Figure 3a shows the elemental composition obtained by XPS analysis for the samples carbonized at various temperatures. (For the spectra of C 1s and O 1s and integration, see Figure S4 and S5, Supporting Information). While the carbon content is increasing

in a stepwise manner from CuAgC₅₀₀ with 57.5 at% to CuAgC₁₀₀₀ with 91.4 at%, a decrease in the oxygen ratio from around 10 at% at 500 °C to about 5 at% at 600 °C was found, followed by constant values around 2.9 (± 0.8) at%. The overall nitrogen content remains almost the same at around 20.2 at% from 500 to 700 °C and then decreases linearly until only 5.4 at% is detected at 1000 °C. These results are in line with the above-discussed TGA measurement of CuAgC_{Stab} under Ar/H₂ and Ar flow (Figure 2c) and very well reflect the temperature segmentation for the evaporation of the different functional groups from the carbon structure.

Besides the elemental composition, the nitrogen-containing functional groups are especially of interest due to the lithiophilic characteristics of nitrogen. As investigated by L.G. Bulusheva et al. via density functional theory calculations, pyridinic-bonded nitrogen, for example, has the strongest interaction with Li ions, increasing the risk of irreversible lithium bonding.^[45] The high

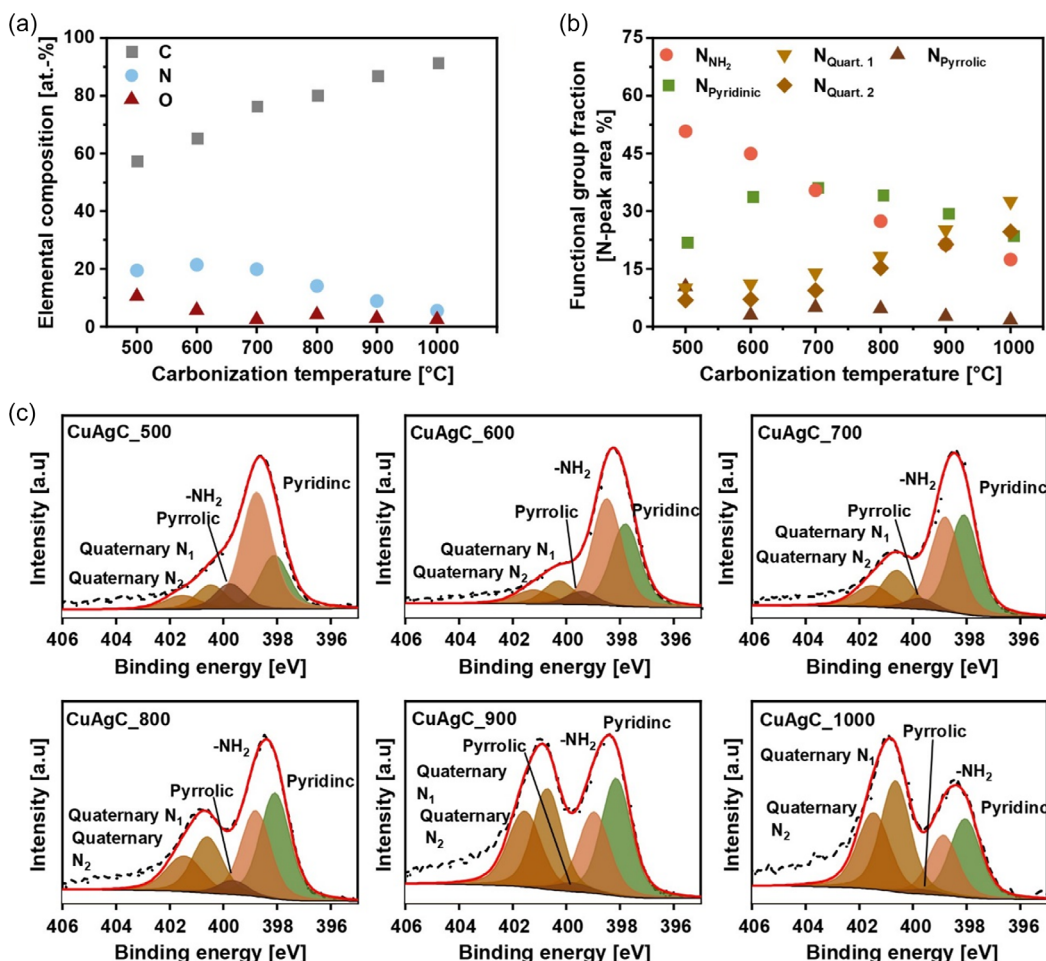


Figure 3. a) XPS analysis of the C 1s, N 1s, and O 1s spectra to evaluate the elemental composition of CuAgC_{500–1000 °C} and in b) a comparison of the N 1s functional group fractions at the different carbonization temperatures. The nitrogen-containing functional group fractions are normalized to the nitrogen peak area c) N 1s XPS spectra for CuAgC_x (x = 500–1000 °C). All spectra are normalized to the highest peak and set to 1. The Ag 3d_{5/2} signal at 368.2 eV was used as the reference (Figure S6, Supporting Information).

lithiophilicity of pyridinic nitrogen originates from the additional lone-pair electrons in the structure. These extra pairs of electrons enable the pyridinic nitrogen containing carbon fibers to act as electron-rich donors with occupied *p*-orbitals. Thus, Lewis base sites are created in the fibers, which adsorb Lewis acidic Li ions through acid–base interactions.^[46] Therefore, the nitrogen-containing functional groups present in each sample can affect the Li deposition. Figure 3b visualizes a comparison of the different nitrogen-containing functional groups for the different carbonization temperatures, which were gained from the analysis of the N 1s spectra in Figure 3c. The spectra for CuAgC₅₀₀, CuAgC₆₀₀, CuAgC₇₀₀, and CuAgC₈₀₀ contain a total of five signals. The signals at 401.6 and 400.5 eV originate from quaternary nitrogen at different positions,^[47] while the signal at 399.8 eV can be assigned to pyrrolic nitrogen.^[48] The peaks at 398.8 and 398.1 eV are associated with $-NH_2$ and pyridinic nitrogen.^[49,50] In contrast, the spectra of CuAgC₉₀₀ and CuAgC₁₀₀₀ do not show any pyrrolic nitrogen at 399.8 eV, as a result of the increased carbonization temperature, whereby

pyrrolic nitrogen was completely removed in the form of N₂, NO, or HCN. The $-NH_2$ bound moieties are normally not reported for carbon fibers but might originate from the reduction at 500 °C under Ar/H₂ flow. As can be seen in Figure 3b, while the number of $-NH_2$ moieties is stepwise decreasing from 50.7 N-peak % for CuAgC₅₀₀ to 17.5 N-peak % for CuAgC₁₀₀₀, the number of both quaternary nitrogen groups is rising with increasing carbonization temperature, confirming the discussed EPR and Raman results, indicating a higher degree in the cyclization of carbon at greater temperatures. The proportion of pyridinic bound nitrogen shows a maximum at 700 °C (36.2 N-peak area %) and then decreases for CuAgC₁₀₀₀ (23.7 N-peak area %) to almost the same ratio as for CuAgC₅₀₀ (22.0 N-peak area %). Multiplying the total nitrogen content from Figure 3a to the nitrogen-containing functional group, the contribution to the whole atomic surface composition is received, as shown in Figure S7, Supporting Information. In contrast to the data in Figure 3b, observations indicate that the absolute quantity of quaternary nitrogen groups exhibits a maximum at temperatures of

700 and 800 °C. However, their proportion relative to the overall surface atom count remains below 4 at% and consequently is unlikely to influence Li deposition significantly. In addition, it should be noted that the calculation of atomic weight fractions from relative sensitivity factors for species with small overall concentrations has a fairly large error of up to several percent. This further restricts the interpretation of a critical contribution to the deposition of Li.

Besides the functional groups, the porous structure of the carbon fibers will also influence Li growth by reducing the local current density and providing more active Li nucleation sites over a larger surface area, thereby changing the Li host properties of the 3D dual metal carbon fibers. Figure 4a depicts the gained isotherms from the static Ar adsorption measurements at 87 K. For clarity, only the adsorption curves are shown, and the corresponding desorption curves can be found in Figure S8, Supporting Information. For carbonization temperatures of 500–900 °C, adsorption curves known as type II isotherms are visible. Type II isotherms are expected for nonporous materials or materials with pore sizes below the accessibility of Ar.^[51] In addition, the shape of all curves is very similar, and the adsorbed volume of Ar is around 7.2 cm³ g⁻¹ at 1000 mbar without a carbonization temperature-dependent specific trend. In contrast, the isotherm of CuAgC₁₀₀₀ shows a nonequibrated type I (b) isotherm because the desorption branch does not meet the adsorption curve

again at low relative pressures (Figure S8, Supporting Information), even though the Ar adsorption measurements were performed under the highest technically possible equilibration settings. According to Cychosz et al. this pseudoirreversibility is caused by the kinetic hindrance of the Ar adsorption affected by materials with ultramicropores smaller than 0.45 nm.^[52] However, type I (b) isotherms are given by materials with micropores at a broader range around (<≈2.5 nm), allowing Ar adsorption.^[51] The steep uptake at low p/p_0 values is caused by the enhanced interaction between Ar and CuAgC₁₀₀₀ in narrow micropores, leading to a pore filling at low p/p_0 .^[51] CuAgC₁₀₀₀ contains, therefore, both narrow ultramicropores and larger micropores.

Furthermore, the adsorbed Ar volume of CuAgC₁₀₀₀ is increased roughly five times (47.5 cm³ g⁻¹ at 1000 mbar) compared to the material carbonized from 500 to 900 °C. The calculated Brunauer–Emmett–Teller (BET)-specific surface areas from the Ar adsorption isotherms are displayed in Figure 4b. For CuAgC_{*x*} ($x = 500–900$ °C), the specific surface areas remain below 10 m² g⁻¹ and, therefore, correspond to the geometrical surface of the fibers. For CuAgC₁₀₀₀, a significantly higher BET surface area of ≈106 m² g⁻¹ is received. Even if this value can only be regarded as a rough estimate, as the adsorption and desorption curves are not in equilibrium, it can be concluded that a significantly higher specific surface area

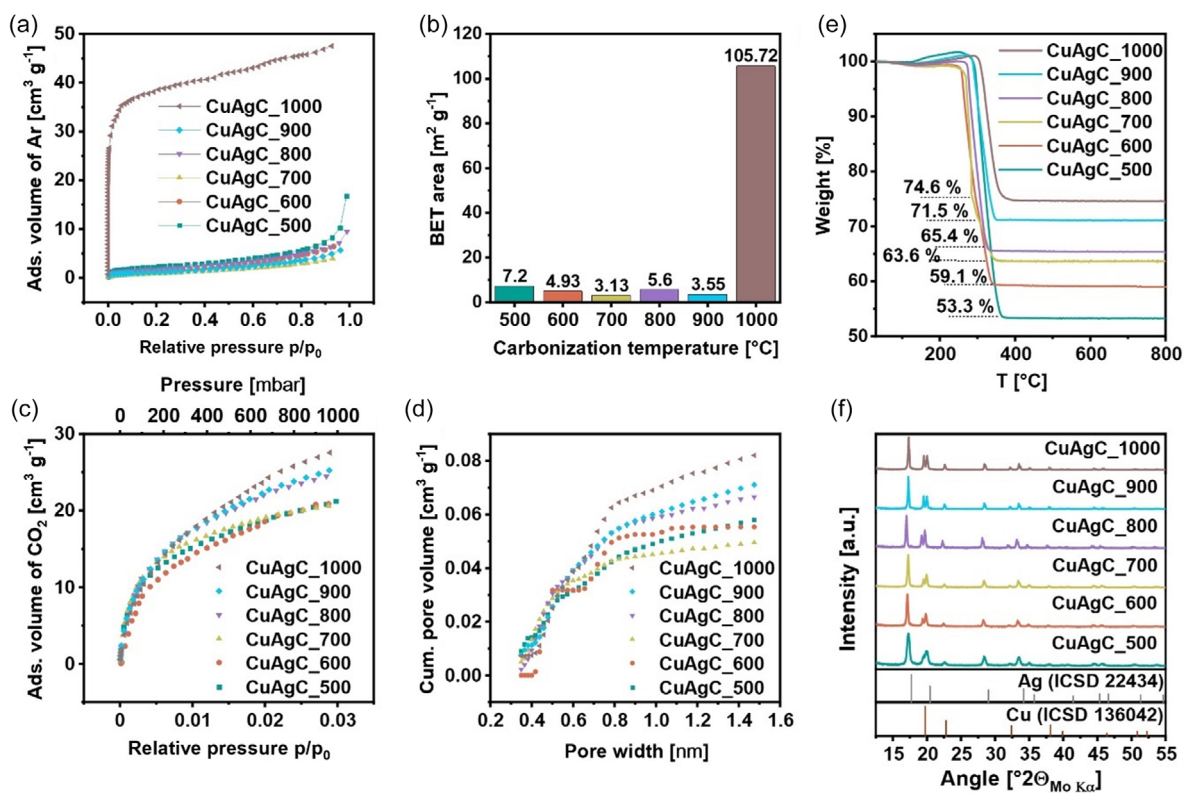


Figure 4. a) Ar adsorption isotherms of CuAgC_{*x*} ($x = 500–1000$ °C) measured at 87 K and in b) the calculated BET area. c) CO₂ adsorption isotherms measured at 273.15 K of the dual metal carbon fibers carbonized from 500 to 1000 °C and in d) the calculated cumulative pore volume by Monte Carlo simulations. e) TGA curves of CuAgC_{*x*} ($x = 500–1000$ °C) measured under atmosphere from 30 to 800 °C. f) XRD pattern of CuAgC_{*x*} ($x = 500–1000$ °C) measured with Mo K α radiation in reflection mode showing Cu and Ag reflections. The reference XRD patterns are Cu (ICSD 136042) and Ag (ICSD 22434).

with larger pore sizes is obtained at a carbonization temperature of 1000 °C.

To analyze the microporous structure of the fibers, CO₂ adsorption isotherms were measured at 273 K because Ar could not infiltrate the minute pores of the CuAgC_x samples, particularly those obtained from 500 to 900 °C. The CO₂ adsorption and desorption curves of these samples are visualized in Figure 4c and S9, Supporting Information, respectively. For all materials, a steep increase in the amount of adsorbed CO₂ at relatively low pressures is visible. However, from 180 mbar, the increase in the adsorbed amount of CO₂ is lower for CuAgC₅₀₀, CuAgC₆₀₀, and CuAgC₇₀₀, respectively, leading to an adsorbed CO₂ volume for all three materials of 21 cm³ g⁻¹ at 1 bar. In comparison, the adsorbed amount of CO₂ on materials carbonized from 800 to 1000 °C keeps increasing even at higher relative pressures, resulting in 24, 25, and 28 cm³ g⁻¹ adsorbed CO₂ volume at 1 bar. The cumulative pore size distribution, illustrated in Figure 4d, was calculated from the CO₂ isotherms by standard Monte Carlo (MC) simulations. For all materials, most pores exhibit a size below 0.7 nm and, therefore, can be categorized as ultramicroporous materials. After the initial steep rise until a pore width of 0.7 nm, a slow increase for the cumulative pore size distribution curves is received. This pattern indicates that all materials exhibit supermicropores (0.7–1.5 nm), albeit in smaller quantities.^[51] The highest pore volume of 0.082 cm³ g⁻¹ is observed for CuAgC₁₀₀₀. Decreasing the carbonization temperature makes a stepwise decline in the total pore volume for CuAgC₉₀₀ and CuAgC₈₀₀ with 0.071 and 0.067 cm³ g⁻¹ visible. The reduction in pore volume at carbonization temperatures of 900 and 800 °C is most likely due to an increasing fraction of heteroatoms, affecting the graphitic interlayer spaces of the carbon and thereby reducing the porosity.^[53] For carbonization temperatures below 800 °C, this trend does not continue, leading to almost the same total pore volume for CuAgC₅₀₀ and CuAgC₆₀₀ of 0.057 and 0.055 cm³ g⁻¹. The calculated MC simulation surface areas are illustrated in Figure S10, Supporting Information, and show, in general, the same trend as the BET areas (Figure 4b). However, due to the identification of ultra- and supermicropores, the micropore MC simulation surface areas of the dual metal carbon fibers are much higher compared to the BET areas in Figure 4b, starting at already 209 m² g⁻¹ for CuAgC₅₀₀ and reaching 269 m² g⁻¹ for CuAgC₁₀₀₀.

Beyond the carbon structure, the embedded metal particles play a crucial role in the deposition of Li due to the strong lithiophilic and lithiophobic properties of Ag and Cu, respectively. To determine the carbon-to-metal ratio of dual metal carbon fibers carbonized at different temperatures, TGA measurements were conducted in an ambient atmosphere, and the results are shown in Figure 4e. All TGA curves exhibit a plateau from 375 to 800 °C, with a gradual rise in residual mass as the carbonization temperature increases, indicating metal percentages of ≈50 wt% for CuAgC₅₀₀, 60 wt% for CuAgC₆₀₀, 64 wt% for CuAgC₇₀₀, 65 wt% for CuAgC₈₀₀, 72 wt% for CuAgC₉₀₀, and 75 wt% for CuAgC₁₀₀₀. The oxidation of the copper occurs continuously from 350 to 800 °C and is therefore not visible within the TGA curves.^[54]

The presence of Ag and Cu particles, as well as the appearance of disordered carbon for all applied carbonization temperatures,

was confirmed by X-ray diffraction (XRD) measurements. The XRD patterns of CuAgC_x (500–1000 °C) depicted in Figure 4f show reflections characteristic for Ag at 17.6°, 20.3°, 28.9°, 34.0°, 35.6°, and for Cu at 19.6°, 22.6°, 32.3°, and 38.0°. The amorphous carbon structure for all samples is evidenced by the missing graphite reflection. This is beneficial in reducing the probability of Li dendrite formation because amorphous carbon results in a more isotropic Li-ion flow with a less concentrated electron distribution than highly ordered graphitic carbon.^[55]

Scanning electron microscope (SEM) was employed to investigate the morphology features of the prepared dual metal carbon fibers. As depicted in Figure 5a, all materials display a porous 3D network with fiber oriented in various directions, with an average fiber diameter between 500 and 600 nm. For the particle size, a clear increase from 600 to 700 °C is observed. Figure 5b shows a large variation in fiber diameter, which is expected from the applied electrospinning process.^[56] Scanning transmission electron microscopy (STEM) coupled with energy-dispersive X-ray spectroscopy (EDS) mapping was employed to investigate the element distribution and particle size of the dual metal carbon fibers. In Figure 5c, bright contrast spots are visible in the high-angle annular dark-field (HAADF) (114–200 mrad) images, indicating metal particles. While for the material carbonized at 500 and 600 °C, only small particles within the fiber are visible, starting from 700 °C, big agglomerates on the surface and between the individual fibers are observed. Therefore, the metal particles can be distinguished into two groups: those located within the individual fibers and those agglomerated on their surface. For the agglomerates on the surface and between the individual fibers, a linear rise in particle size with increasing the carbonization temperatures from 700 to 1000 °C is noticeable, as shown by the particle size distribution in Figure S11, Supporting Information. The average particle surface area is around 0.109 μm² for CuAgC₇₀₀, 0.119 μm² for CuAgC₈₀₀, 0.169 μm² for CuAgC₉₀₀, and 0.342 μm² for CuAgC₁₀₀₀. Thereby, the EDS maps in Figure 5d confirm that the formed agglomerates are CuAg Janus particles.

Bright-field (BF) images and elemental STEM-EDS maps of Cu and Ag, illustrated in Figure 6a, are taken to investigate the particle size and distribution of the small metal particles situated within the individual fibers. The STEM BF images from 500 to 700 °C show larger nanoparticles ranging from 50 to 200 nm aligned along the fiber center and smaller nanoparticles distributed on the fiber surface. (As the BF and HAADF contrast is not only Z but also thickness dependent, a discrimination between Ag and Cu only on the basis of contrast is not feasible.) For CuAg₇₀₀, the particle distribution has changed to the extent that the alignment of larger particles along the center of the fiber is no longer clear anymore, and there are fewer small particles on the fiber surface. For carbonization temperatures above 700 °C, especially 900 and 1000 °C, the alignment of particles along the fiber center gets more dominant and particles grow in size. Moreover, fewer smaller particles on the fiber are observed compared with the samples carbonized at low temperatures. The STEM-EDS maps indicate that the larger particles aligned along the fiber center of CuAgC₅₀₀, CuAgC₆₀₀, and CuAgC₇₀₀ correspond mainly to Ag and Cu is more present on the outside. This is changing for CuAgC₈₀₀, CuAgC₉₀₀, and

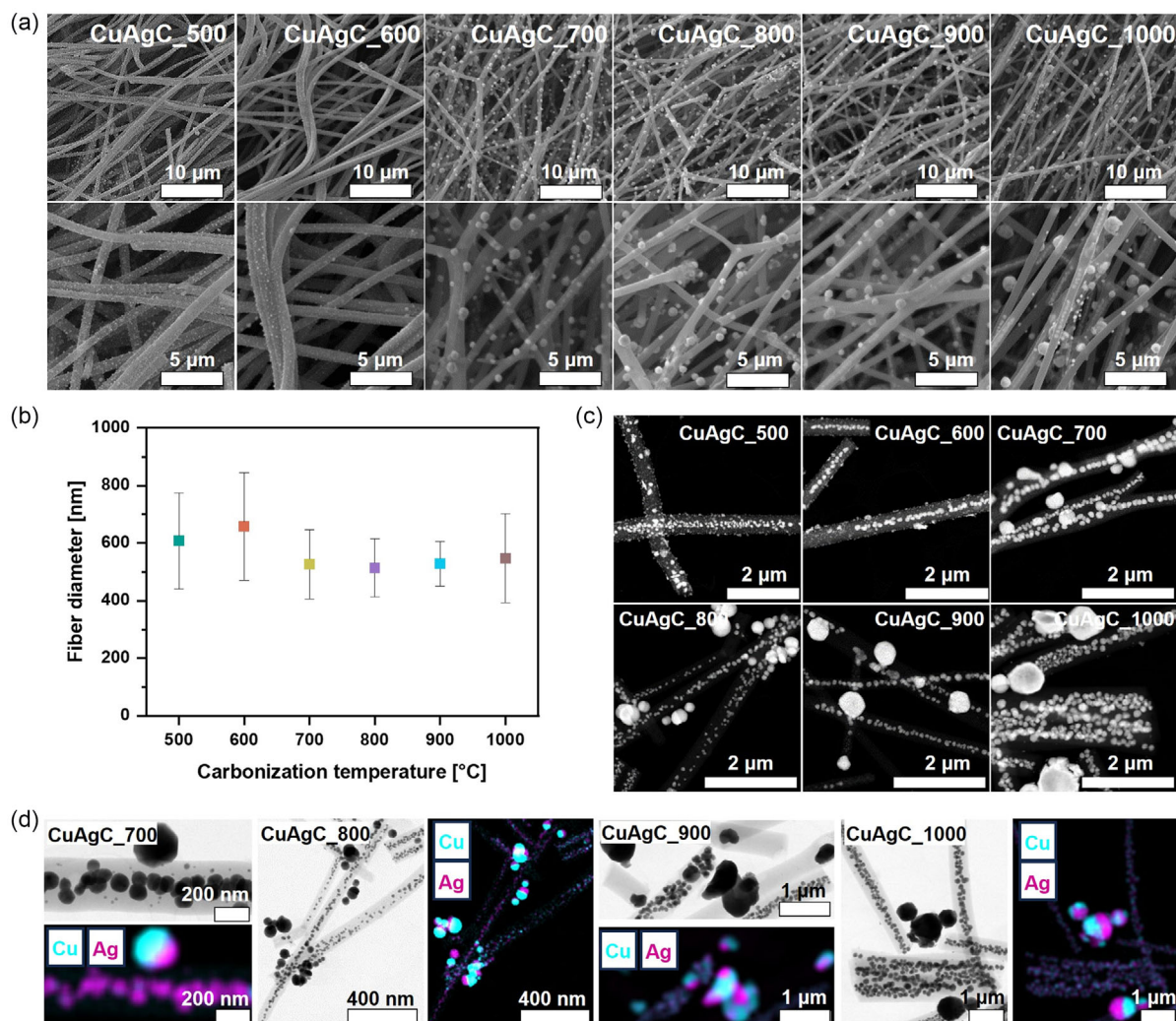


Figure 5. a) SEM images of CuAgC_x ($x = 500\text{--}1000\text{ }^{\circ}\text{C}$) showing a porous fiber network with carbonization temperature-dependent particle sizes. b) Average fiber diameter of CuAgC_x ($x = 500\text{--}1000\text{ }^{\circ}\text{C}$), showing mean value and error bar with \pm standard deviation (SD) for a sample quantity (n) of $n = 50$. c) STEM HAADF images showing big metal agglomerates on the surface and between the individual fibers for materials carbonized from 700 to 1000 °C. d) BF images and the corresponding STEM-EDS color maps of Cu and Ag for fibers carbonized from 700 to 1000 °C.

CuAgC₁₀₀₀, where both Ag and Cu are found along the fiber center.

The change in the radial metal particle distribution is highlighted by the corresponding line profiles in Figure 6b and S12, Supporting Information, visualizes how line-profiles were extracted on the example of CuAgC₉₀₀. The change of the Cu line shape from a flattened broad curve spanning the whole width of the carbon fiber toward a sharp peak with increasing carbonization temperature demonstrates the accumulation of Cu particles at the center of each fiber. Meanwhile, for CuAgC₅₀₀ and CuAgC₆₀₀, Cu particles are uniformly distributed throughout the whole fiber, with a slight concentration on the fiber surface. Ag particles are mainly centered at the core, with some particles on the carbon fiber surface, creating a lithiophilic–lithiophobic gradient on each single fiber. Starting at 700 °C (CuAgC₇₀₀), the gradient starts to vanish, and the small peaks at the fiber surface for both Cu and Ag disappear.

For carbonization temperatures of 800, 900, and 1000 °C, both Ag and Cu are mainly distributed along the fiber center and the lithiophilic–lithiophobic gradient disappeared completely. In addition, a stepwise overall shift of the metal particles from the surface toward the center can be observed for carbonization temperatures of 500–800 °C. Afterward, the centered distribution of Cu and Ag stays consistent and only a change in the particle size is noticeable. Also, the overall amount of metal content increases according to the TGA analysis in Figure 4e.

As visible in Figure 6c, the constant growth of the particle sizes with increasing carbonization temperature can directly be observed by the changing shape of the cumulative particle size curve from a right-hand to a left-hand curve. While for CuAgC₅₀₀ and CuAgC₆₀₀ the majority of Cu particles possess a surface area below 1000 nm², a shift toward particle sizes of $\leq 2000\text{ nm}^2$ can be seen for 700 °C and a uniform distribution from ≤ 3000 to $\leq 7000\text{ nm}^2$ is obtained for the dual metal carbon

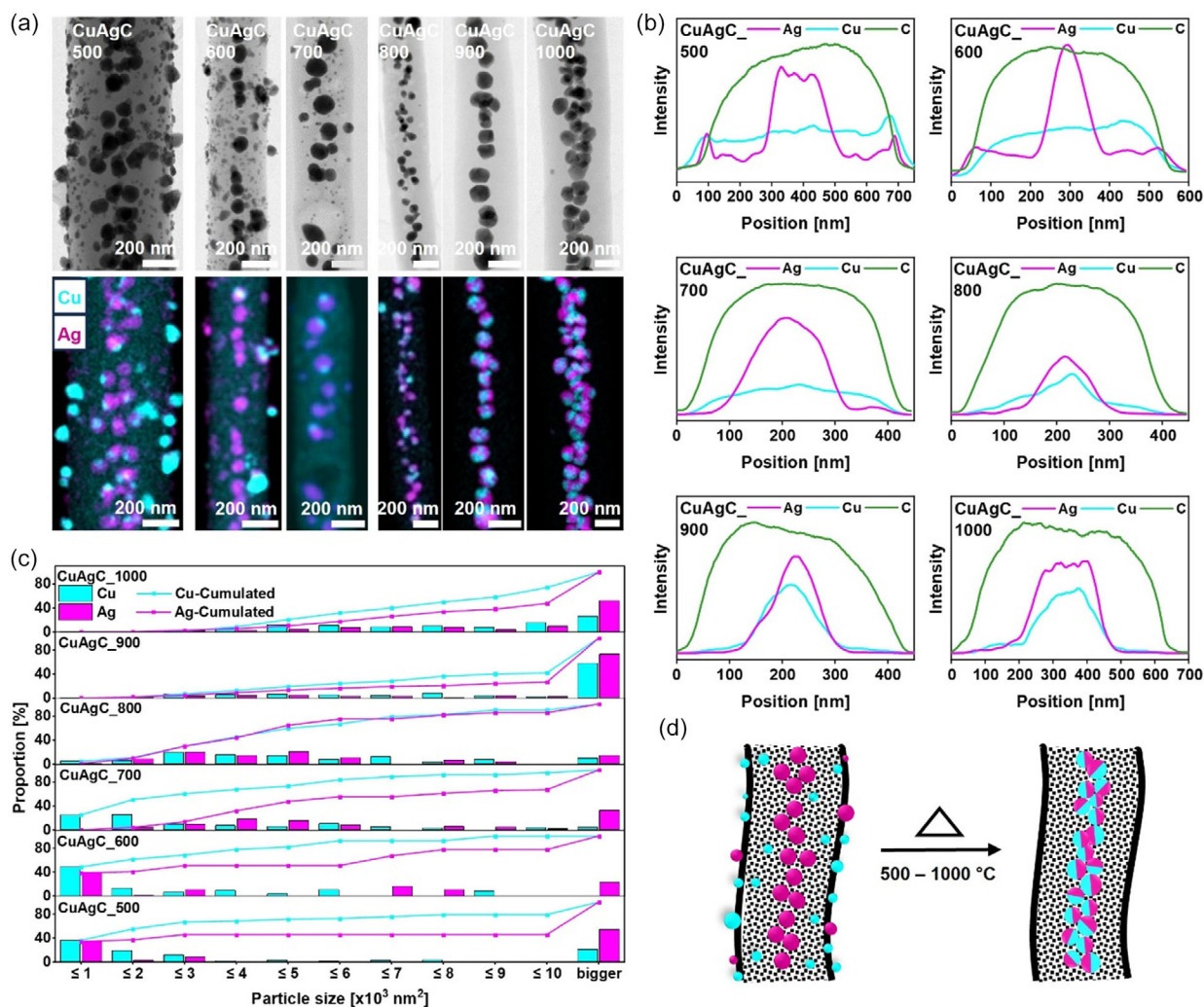


Figure 6. a) STEM BF images of a single CuAgC_x ($x=500\text{--}1000\text{ }^{\circ}\text{C}$) fiber (upper row) and the corresponding elemental EDS maps of Cu and Ag (lower row). b) Analysis of the elemental distribution of C, Cu, and Ag by measuring line-profiles of the individual fibers shown in a). c) Absolute and cumulative particle size of Cu and Ag carbonized from 500 to 1000 °C, with a sample quantity $n=2565$ for CuAgC₅₀₀, $n=2373$ for CuAgC₆₀₀, $n=1523$ for CuAgC₇₀₀, $n=311$ for CuAgC₈₀₀, $n=226$ for CuAgC₉₀₀, and $n=110$ for CuAgC₁₀₀₀. d) Schematic illustration of the change in size and distribution of Cu and Ag with increasing carbonization temperature.

fibers carbonized at 800 °C. Upon final increase of the carbonization temperature to 900 and 1000 °C, most Cu particles undergo substantial growth, attaining sizes commensurate with those of Ag particles and exceeding 10 000 nm² in area. A similar trend is observable for the silver particles dispersed within the carbon fibers initially. Notably, the centrally located linear arranged Ag particles already exceed surface areas of 10 000 nm² for carbonization temperatures of 500 °C.

The centered, linear arranged Ag particles, in combination with the small Cu and some Ag particles on the fiber surface, create a lithiophilic–lithiophobic gradient at carbonization temperatures of 500 and 600 °C. This arrangement results from the different precipitation processes of the used metallic precursors. CuAc and AgNO₃ were mixed with PAN in *N,N*-dimethylformamide (DMF) to generate the electrospinning solution. While CuAc dissociates in the solution, Ag particles are formed immediately due to

the reduction by DMF.^[57,58] Polymer encapsulation of Ag particles occurs in the solution and causes the linear arrangement during the high voltage electrospinning process.^[59] While the slow reduction rate of Ag⁺ restricts the complete precipitation of silver particles, residual AgNO₃ remains dissolved in the solution in small quantities. The decomposition of the organic components (acetate and nitrates) and the formation of Cu and Ag particles occurs during the subsequent heat treatments, first at 250 °C in the air, followed by the reduction step at 500 °C under Ar/H₂ flow and the different carbonization procedures (600°–1000°) under Ar flow, whereby gases such as CO₂, NO₂, NO, O₂, and acetone are released.^[35] The subsequent movement of the homogeneously distributed Cu particles from the surface toward the center results from the different particle sizes of Cu and Ag. Due to the smaller particle size of Cu, the melting process precedes at elevated temperatures first. The increased particle mobility of Cu induces

movement of the small Cu particles toward the bigger centered Ag particles. The Cu and Ag particles then diffuse across their interfaces and encourage the establishment of new atomic bonds between the two particles, consequently forming CuAg Janus particles (Figure S13, Supporting Information) at carbonization temperatures above 700 °C. As some small Ag particles were also located on the fiber surface, the formation of CuAg Janus agglomerates on the surface of individual fibers already occurs at 700 °C, as visible in Figure 5d.^[60] The temperature threshold for forming CuAg Janus particles aligns with the Cu–Ag phase diagram, which indicates an equilibrium point at 779 °C.^[60] The identified changes in particle size and distribution within individual fibers at rising carbonization temperatures are schematically summarized in Figure 6d. In addition, Figure S14–S19, Supporting Information, show the HAADF (114–200 mrad) images and the corresponding STEM-EDS maps of C, N, and O for each carbonization temperature. The distribution of C, N, and O is uniform at all carbonization temperatures applied.

The impact of the structural changes of the dual metal carbon fibers with increasing carbonization temperature is tested in cells against Li metal as the reference and counter electrode, while the dual metal carbon fibers are used as working electrodes and directly placed on a planar Cu-foil current collector.

Initially, Li plating was performed at a current density of 0.1 mA cm⁻² for 25 h, followed by stripping until reaching 0.2 V at a current density of 0.1 mA cm⁻². Subsequently, the current density was increased to 0.5 mA cm⁻² for both Li plating and stripping, while the duration of Li plating was changed to 5 h. The high areal capacity of 2.5 mA cm⁻² per cycle ensures a fast evaluation of the cycling stability due to the increased possibility of Li dendrite formation and enables a rapid observation of distinctions among the carbonized dual metal carbon fibers. The different cycling lifetimes are visualized in Figure 7a. While it can be directly seen that CuAgC₇₀₀ possesses the longest cycling stability with over 1100 h, the zoomed-in sections in Figure 7b highlight the cell failure of the other carbonization temperatures. For CuAgC₅₀₀ and CuAgC₆₀₀, the cells exhibit stable cycling for around 250 and 270 h. After the threshold value of 700 °C, a gradual reduction in cycle stability is observed with increasing carbonization temperatures until 900 °C, leading to a cell lifetime of 850 h for CuAgC₈₀₀ and 760 h for CuAgC₉₀₀. Subsequently, CuAgC₁₀₀₀ shows an improved Li plating/stripping stability of around 990 h, indicating different Li deposition mechanisms according to the existing structural properties of the used dual metal carbon fibers, respectively.

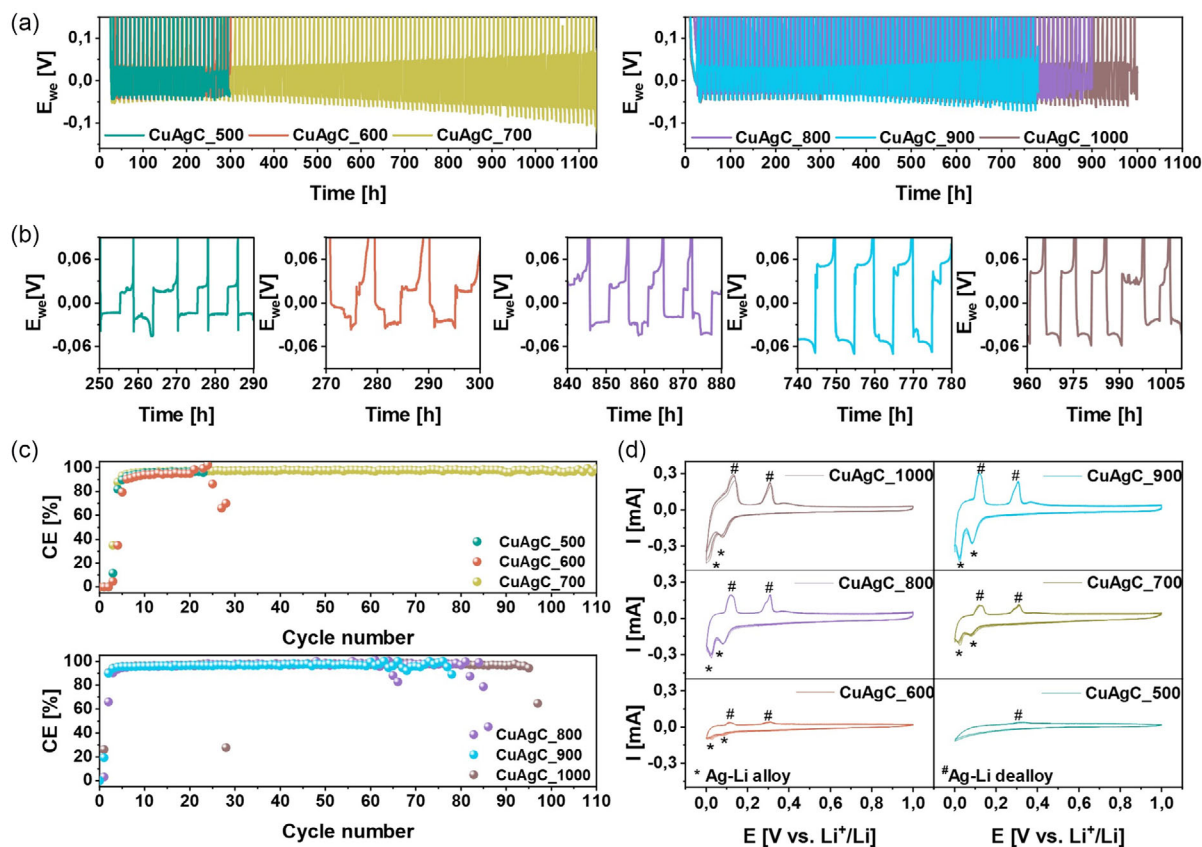


Figure 7. a) Voltage profiles of CuAgC_x ($x = 500\text{--}1000$ °C) during Li plating/stripping tests. b) The zoomed-in sections of cell failure for CuAgC₅₀₀, CuAgC₆₀₀, CuAgC₈₀₀, CuAgC₉₀₀, and CuAgC₁₀₀₀ (from left to right). c) The relevant CE according to the performed Li plating/stripping tests in a). All tests were performed in a cell configuration of Cu-foil/sample|electrolyte|Li metal. Initially, Li plating was conducted at 0.1 mA cm⁻² for 25 h and stripped until 0.2 V at 0.1 mA cm⁻². Subsequent Li plating was performed at 0.5 mA cm⁻² for 5 h, followed by Li stripping until 0.2 V without a time limitation. d) CV curves of CuAgC_x ($x = 500\text{--}1000$ °C) from 0 V to 1 V at a scan rate of 0.01 mV s⁻¹.

Further, the rate performance was investigated by raising the current area density during Li plating from 0.1 to 7 mA cm⁻² [(0.1, 0.2, 0.5, 1.0, 1.5, 2.0, 2.5, 3.0, 3.5, 4.0, 4.5, 5.0, 6.0, 7.0) mA cm⁻²] after every five cycles, as can be seen in Figure S20, Supporting Information. To investigate the influence of the current density, the Li plating capacity was fixed to 2.5 mA h cm⁻². Consistent with the cycling performance observed in Figure 7a,b, only CuAgC_700 could sustain cycling up to a current density of 6 mA cm⁻². Samples carbonized at lower temperatures of 500 and 600 °C exhibited reduced current density stabilities, with a maximum of 3.5 or 2.5 mA cm⁻². In contrast, samples carbonized at elevated temperatures between 800 and 1000 °C demonstrated the onset of Li dendrite formation at 4 and 3.5 mA cm⁻², respectively. The determined threshold value for CuAgC_700 underlines the significant relationship of a harmonized electron and ion transport mechanism to receive long-term stabilities and fast charging conditions. In accordance with Sand's equation (Equation (S1), Supporting Information), Sand's time, which denotes the onset of lithium dendrite formation, decreases as the applied current density increases, raising the probability of concentrated Li deposition at elevated current densities.^[61] Therefore, achieving stable Li metal anodes under fast charging emphasizes the critical importance of rapid charge-transfer kinetics and uniform ion diffusion rates to prolong the onset of Li dendrite formation.

The received Coulombic efficiencies (CE) are illustrated in Figure 7c. The initial CE, which can be seen in Table S2, Supporting Information, shows a value <2% for all carbonization temperatures resulting from passivation processes, including SEI formation and, most importantly, the irreversible interaction of Li ions and "defect sites" caused by heteroatoms of N, H, and O and functional groups like pyridinic bonded nitrogen or carbonyls (C=O) in the dual metal carbon structure. Due to the formation of SEI at the beginning of Li plating, Li ions are irreversibly bonded, hindering efficient Li stripping at the first cycle. However, a linear increase in efficiency can be noticed with rising carbonization temperatures. While at low carbonization temperatures of 500 and 600 °C CE of more than 90 % are only achieved after five cycles, four cycles are required for CuAgC_700. With further increases in carbonization temperatures, three cycles are required for CuAgC_800 and two cycles for CuAgC_900 and CuAgC_1000 before CE values exceed 90%. The decreasing number of cycles with increasing carbonization temperature to reach high CE values results from the different carbon structures, as shown in Figure 2 and 3. The high amount of heteroatoms and functional groups in fibers, especially carbonized at low temperatures (500–700 °C), induces high irreversible Li-ion binding and inhibits Li stripping until these defect sites are occupied. The linearly decreasing amount of heteroatoms at increasing carbonization temperatures leads to progressively lower irreversible Li-ion bindings, rising initial CE. After the first cycles, the average CE of all materials is 96–97% until cell failure, implying no difference in the efficiency of the charge transfer processes during long-term cycling between the individual samples.^[62]

Cycling voltammetry (CV) curves in Figure 7d visualize an increased current response with rising the carbonization temperature for the two oxidation peaks at 0.12 and 0.3 V and the reduction peaks at 0.02 and 0.08 V. The oxidation peaks describe the

Ag–Li dealloying and the reduction peaks the Ag–Li alloying reaction. Therefore, the increase in the current response indicates enhanced accessibility for the Ag–Li alloy/dealloy formation at higher carbonization temperatures.^[63] The absence of dealloying peaks for CuAgC_500 underlines the weak interaction of Li ions with the lithiophilic Ag particles, mainly caused by the high electrical resistances (Figure 1c), whereby Li ions are preferably deposited on the Cu-foil current collector. With decreasing electrical resistance, the rise in the current response becomes apparent, causing the expectation of a preferred interaction between the lithiophilic Ag particles and the Li ions. In addition, a shoulder at 0.08 V of the oxidative peak at 0.12 V is visible for CuAgC_1000, indicating enhanced Li-ion adsorption properties. The shoulder at 0.08 V describes Li_xC desorption and the reduction peak at 0.1 V corresponds to Li_xC adsorption.^[64] The increased surface area of CuAgC_1000, as determined by the BET area in Figure 4b, implies further reduced local current densities by offering significantly more active sites for Li-ion adsorption on the surface of the fibers. Furthermore, electrolyte diffusion pathways are shortened, leading to more homogenized Li-ion transport kinetics.^[65] This structural difference causes the increased cycling stability of CuAgC_1000 compared to 900 and 800 °C because an enhanced use of the soft carbon Li host properties is possible.

SEM pictures after cycling were recorded to prove the preferred Li precipitation as indicated by the CV curves. Therefore, images of CuAgC_x ($x = 500\text{--}1000$ °C) facing the separator side (cf., front) and facing the Cu-foil current collector (cf., back) were taken, as can be seen in Figure 8a. In addition, Figure 8b schematically describes the preferred Li deposition at the different carbonization temperatures. As depicted in Figure 8a, at CuAgC_500 and CuAgC_600, Li ions prefer to be deposited at the Cu current collector. While for CuAgC_500, the formation of concentrated mossy Li spots is visible, a more homogenous Li plating between the back side of the fibers and the Cu-foil current collector is indicated by the images of CuAgC_600. However, due to the disordered carbon structure, characterized by a low degree of aromatization and a high concentration of surface heteroatoms (e.g., nitrogen and oxygen), as shown in Figure 1–3, both carbonization temperatures exhibit high electrical resistance. This causes a lousy electron supply within the carbon skeleton and a strong electron concentration gradient between the highly electrically conductive Cu-foil current collector and the dual metal carbon fibers. As a result, the electrical field is concentrated at the interface between the Cu-foil and the dual metal carbon fibers, driving the Li nucleation toward the back side. The liquid electrolyte and the high porosity of the dual metal carbon fibers give a continuous Li deposition at the Cu-foil. Simultaneously, excess Li ions, particularly in the initial cycles, are consumed by occupying defect sites within the dual metal carbon fibers. In addition, the limited electron availability within the dual metal carbon fibers affects the reaction, which primarily occurs at the Ag particles located at the interface of the carbon fibers and the Cu-foil current collector. Here, the electrical resistance is reduced due to the direct contact with the highly conductive Cu-foil. Nevertheless, caused by the slow electron transport within the dual metal carbon fibers, most of the promising lithiophilic–lithiophobic gradient within the high resistance carbon structure is not accessible for Li ions, resulting

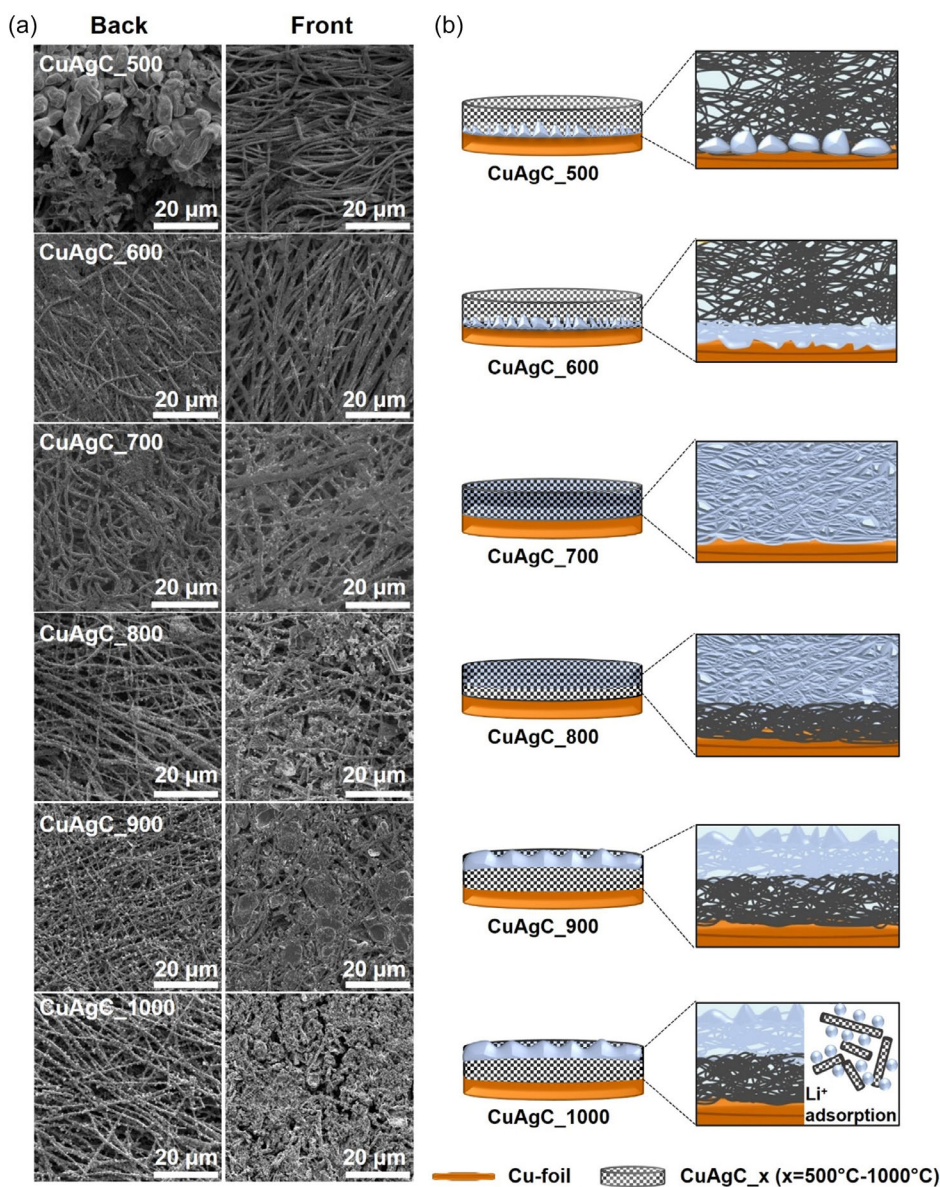


Figure 8. a) SEM pictures of lithiated CuAgC_x ($x = 500\text{--}1000^\circ\text{C}$) after ten cycles at a Li plating capacity of 2.5 mA cm^{-2} . “Front” labels the CuAgC_x side facing the separator, while “Back” describes the side facing the Cu-foil current collector. b) Schematic illustration of the preferred Li deposition at the corresponding carbonization temperatures.

in fast cell failure, low rate performance, and less pronounced Ag–Li alloy reaction as shown in Figure 7a,d and S20, Supporting Information.

Upon reaching the threshold value CuAgC_{700} , the preferential deposition of Li at the back side of the fibers becomes imperceptible, replaced by a highly homogeneous Li deposition observed throughout the entire dual metal carbon fibers. As both sides show an almost equal homogenous swelling of the fibers by around 780 nm, the Li deposition can be explained as follows. Owing to the substantially reduced electrical resistance of CuAgC_{700} , the electron concentration gradient between the Cu-foil and the dual metal carbon fibers becomes less pronounced, facilitating rapid electron transport sufficient to

promote Li nucleation at the energetically favorable Ag particles. While the lithiophilic Ag particles are predominantly embedded within the dual metal carbon fibers, most of the lithiophobic Cu particles remain distributed on the surface of the fibers (Figure 6b). The lithiophilic Ag particles enable the migration of Li ions toward the fiber center, whereas the lithiophobic Cu particles inhibit concentrated lithium deposition on the fiber surface.

As a result, the homogenous distributed lithiophilic–lithiophobic gradient on each fiber reduces the ion diffusion pathways. Thereby, the sluggish ion diffusion kinetics, normally leading to top Li deposition in carbon fiber matrix, are overcome.^[26,27] The enhanced ion diffusion kinetics result from

the energetically preferred Ag–Li alloy with a negative Gibbs energy, reducing the intricate kinetic competition between Li-ion transport and interfacial reactions.^[24,27] Even though the already formed CuAg Janus particle on the surface might harm the homogenous Li deposition behavior, the enhanced cycling stabilities and high rate performance, as depicted in Figure 7a and S20, Supporting Information, are attained.

During further cycling, the preferred Li deposition becomes increasingly recognizable at the front side (facing the separator) of the dual metal carbon fibers, as seen in the SEM images in Figure 8a for CuAgC₈₀₀ to CuAgC₁₀₀₀.

As the carbonization temperature further rises to 800 °C, the electrical conductivity of the dual metal carbon fibers increases substantially, leading to a roughly uniform distribution of electrical conductivity across the carbon fibers. Consequently, the dual metal carbon fibers are equipotential, and the ion transport mechanism becomes the critical step for Li deposition. The shortened Li-ion pathways toward the high electrically conductive fibers favor the formation of Li metal at the front side.^[27] In addition, the formation of CuAg Janus agglomerates promotes concentrated Li nucleation and growth at the silver site because less effective surface areas for the Li-ion deposition are available. Additionally, the migration of the lithiophobic Cu particles toward the fiber center compromises the protective function of Cu particles in preventing localized Li deposition on the fiber surface, promoting Li deposition near the separator and increasing the risk of Li dendrite penetration. As a result, cell failure occurs more rapidly, and the rate performance of CuAgC₈₀₀ is lower compared to CuAgC₇₀₀. As the particle growth and agglomeration of Ag and Cu is further increasing from 800 to 900 °C, the risk of Li–dendrite formation is also enhanced. The energetically preferred Ag–Li formation affects a more concentrated Li-ion diffusion toward the big silver particles, supporting the growth of Li dendrites and leading to a shorter cycle lifetime of CuAgC₉₀₀ compared to CuAgC₈₀₀ (Figure 7a). However, for CuAgC₁₀₀₀, the enlarged surface area, as shown by the Ar BET result in Figure 4b, enhances mass transfer kinetics by providing significantly more space for Li adsorption and shortens the electrolyte diffusion pathways.^[65] Consequently, the impact of the Cu and Ag particle movement and growth is minimized, and a more uniform Li-ion transport is achieved, whereby the increase in cycle stability became apparent compared to CuAgC₈₀₀ and CuAgC₉₀₀.

3. Conclusion

The high structural complexity of lithiophilic–lithiophobic 3D dual metal carbon fibers significantly influences the homogenous Li deposition. Therefore, a detailed structural analysis of lithiophilic Ag and lithiophobic Cu containing carbon fibers at different carbonization temperatures was performed to better understand how each factor influences Li deposition behavior. At lower carbonization temperatures, the fibers possess an unordered carbon structure with a high concentration of heteroatoms. At these low carbonization temperatures, the assembly of Cu and Ag particles creates a lithiophilic–lithiophobic gradient within each fiber. However, the high electrical resistance hinders Li-ion interaction with the fibers, forming mossy and dead Li.

On the other hand, higher carbonization temperatures eliminate heteroatoms and promote the development of a more ordered carbon structure. However, these elevated temperatures also cause the agglomeration of Cu and Ag particles at the surface and in the fiber center, leading to the formation of CuAg Janus particles. Consequently, the lithiophilic–lithiophobic gradient is disrupted and concentrated Li deposition on top of the fibers is observed. At a carbonization temperature of 700 °C, a threshold value regarding a homogenous Li deposition was received. The low electrical resistance, in combination with still existing lithiophilic–lithiophobic gradient, enables enhanced cycling stability. These results highlight the importance of the chosen thermal treatment parameters when considering the use of composite carbon-based materials as interlayers in advanced battery configurations, where a homogenous Li-ion deposition is essential.

4. Experimental Section

Synthesis of CuAgC_x ($x = 500–1000$ °C): All chemicals were utilized as received. Initially, 3.776 g of PAN (with an approximate molecular weight of 150 000) and 2.815 g of anhydrous CuAc were dissolved in 40 mL of anhydrous DMF and stirred at room temperature for a duration of one day. Subsequently, 2.633 g of AgNO₃ was introduced into the solution to obtain a molar ratio 1:1 for the metal particles. The solution was stirred for another day until a cyan-colored solution was attained. The electrospinning procedure was executed using the prepared solution on an electrospinner equipped with a horizontally positioned rotating drum collector (IME Medical Electrospinning, The Netherlands) under controlled environmental conditions of 25 °C and 30% relative humidity. The solution was loaded into a syringe and delivered through one needle via an automatic syringe pump at a flow rate of 20 $\mu\text{L min}^{-1}$. The needle, featuring an inner diameter of 0.8 mm, was horizontally displaced at a speed of 20 mm s^{-1} within a range of ± 55 mm and a turn delay of 500 ms. The rotation speed of the drum was set at 700 rpm, and the distance from the collecting drum to the needle tip was maintained at 140 mm. The electrospinning process was conducted at a voltage of 25 kV for a total duration of 6.5 h. The resultant green body underwent cross-linking in ambient air for 15 h at 250 °C, followed by a reduction step under Ar/H₂ (3 vol%) flow for 2.5 h at 500 °C, with a heating rate of 5 °C min^{-1} , leading to CuAgC₅₀₀. The following carbonization step was conducted under a pure Ar flow for 3 h at the respective temperature (600–1000 °C). The oven was cooled naturally to room temperature and the final dual metal carbon fibers were ready to use.

Structural Characterizations: Powder XRD measurements were performed at an EMPYREAN X-ray diffractometer (PANalytical, The Netherlands) with Mo K α radiation in reflection mode. The samples were placed between two non-reflective Kapton foils and measured at 45 kV with a current of 40 mA. The step size is 0.008 from 5° to 55° 2 theta, with a repetition of two. The background was subtracted via HighScore Plus (Malvern Panalytical) and smoothed using the Savitzky–Golay method afterward. As references, XRD pattern Cu (ICSD 136 042)^[66] and Ag (ICSD 22 434)^[67] are used.

BET measurements were applied to specify the surface area by Ar and CO₂ adsorption, and the automatic adsorption analyzer Micro 30 °C-02-Analysis Station (3P Instruments, Germany) was used. MC simulations were conducted to quantify the pore volume, measured by CO₂ adsorption, using Quantachrome ASiQwin-Automated Gas Sorption Data software (Quantachrome, Germany).

Thermogravimetric analyses, coupled with mass spectroscopy, were conducted on a NETZSCH TGA/STA-QMS 403D thermoanalyzer (Germany) at a temperature range of 30–1000 °C and a heating rate of 5 °C min^{-1} under atmosphere, Ar/H₂ (3 vol%) and Ar.

SEM images were taken with FEI Quanta FEG 650 (FEI, USA). A K&W transfer module (Kamrath & Weiss, Germany) was used to transfer the samples from the glove box to the SEM chamber to protect the lithiated samples from air contamination. The module is opened in the evacuated chamber, avoiding exposure to the ambient atmosphere. An acceleration voltage of 2 kV and a spot size of 3 were used for SEM measurements to guarantee the true-to-life morphology and avoid electron beam damage on the sample surface.

STEM measurements were performed at FEI Titan G2 80-200 microscope with a Cs-probe corrector and a HAADF detector.^[68] The microscope was run at 200 kV with a condenser aperture of 70 μm , giving a convergence half angle of 24.7 mrad. Camera length was set to 65 mm, resulting in an acceptance angle of 61 mrad for the BF and 114–200 mrad for the HAADF detector. Elemental maps were recorded by EDS, using four window-less large-solid-angle symmetrical Si drift detectors. The dispersion was adjusted to cover the energy range of 0–20 keV, including Cu K lines at 8.1–8.9 keV, but no Ag K lines at 22.26 keV.

Raman microspectroscopy experiments were conducted with a WITec alpha300R Raman microscope (OXFORD Instruments, UK) using a solid-state excitation laser of 532 nm, a grating of 600 lines mm^{-1} , and a laser power of 1 mW. The spectra were collected with a point focus lens and a 50 \times objective on an area of 100 μm \times 100 μm with 50 points per line and 50 lines per frame. Each spectrum at each point was acquired with an integration time of 2 s. The collected spectra were corrected for cosmic rays and averaged to obtain a representative spectrum for each sample. The spectral parameters were obtained by curve fitting with Origin (Originlab Corporation, 2021, United States) and followed the deconvolution method proposed by Brubaker et al. into five bands.^[39] A Pseudo-Voigt function was used for the D1, D2, and G bands, while the D3 and D4 bands were fitted considering only Gaussian contributions.

EPR measurements were done at 295 K using a Bruker EMX spectrometer operating at 9.64 GHz. Samples were filled into 4 mm (outer diameter) EPR tubes under air. X-band continuous wave EPR spectra were acquired as the first derivatives of absorption spectra with a microwave power of 0.3162 mW, a modulation amplitude of 0.4 mT, and a modulation frequency of 100 kHz. In the case of samples that exhibited the presence of free radicals, spectra were also acquired with a reduced modulation amplitude of 0.05 mT to check for artificial broadening.

XPS was acquired using a K α spectrometer (Thermo Fisher, USA). The device has an Al K α X-ray source and is operated at a base pressure of 10–9 mbar. For measuring the different elements, a pass energy of 50 eV and a spot size of 400 μm on the sample were used. The survey spectrum for each carbonization temperature can be found in Figure S21, Supporting Information, and is measured with a pass energy of 200 eV. All samples were investigated and fitted using the Avantage software (ThermoFisher). The analyzer transmission function, Scofield's sensitivity factors, and effective attenuation lengths for photoelectrons, calculated using the standard TPP-2 M formalism, were used for quantification. For the evaluation of the core peaks, a "smart background" was applied, which is based on a Shirley-type background. A further constraint is applied to ensure that the background is never more intense than the measured data. Voigt profiles with 70% Gaussian and 30% Lorentzian contribution fit all core elements. Furthermore, shake-ups occur at high binding energies in the C 1s and N 1s spectra.

The four-point probe method was used to determine the electrical resistance of the samples. Therefore, the dual metal carbon fibers were cut into rectangles with a side length of 1.5–3 cm, and the thickness was measured at five different spots using a thickness dial gauge (Käfer Messuhrenfabrik, Germany). A Loresta GX with an LSP probe head (Nittoseiko Analytech) was used to measure the electrical resistance. The probe head had a linear electrode arrangement with four electrodes with a distance of 5 mm between each of them. The tip of the electrode pins is rounded with a diameter of 2 mm and placed in the center of the sample. The device automatically calculates the resistivity correction factor and converts the measured resistance into a specific resistivity based on the position of the probe head and the dimensions of the dual metal-carbon fibers using Poisson's equation described in the literature.^[69]

Electrochemical Measurements: To investigate the Li deposition onto the dual metal carbon fibers, Li plating/stripping tests were performed in a battery configuration of Cu-foil/sample|electrolyte|Li metal in CR2032 coin cells with a polypropylene (Celgard 2400) and glass fiber (Whatman) separator. A dual lithium salt carbonation solution, including 0.6 M lithiumtetrafluoroborat, 0.6 M lithiumdifluoro(oxalate)borate in fluoroethylene carbonate, and diethyl carbonate (1:2, vol/vol), was used as electrolyte. First, a formation cycle was applied to all cells, containing Li plating at 0.1 mA cm^{-2} for 24 h and Li stripping until 0.2 V at 0.1 mA cm^{-2} . Subsequently, the current density for Li plating was increased to 0.5 mA cm^{-2} for 5 h and again stripped to 0.2 V at 0.5 mA cm^{-2} , resulting in a high capacity of 2.5 mAh cm^{-2} for each cycle. CV curves were recorded from 0 to 1 V with a scan speed of 0.01 mV s^{-1} . Rate performance measurements involved Li plating twice at 0.1 mA cm^{-2} until a Li plating area capacity of 4.5 mAh cm^{-2} was reached, and then the Li was stripped to 0.6 V at 0.1 mA cm^{-2} . Subsequently, the current density during Li plating was increased stepwise from (0.1, 0.2, 0.5, 1.0, 1.5, 2.0, 2.5, 3.0, 3.5, 4.0, 4.5, 5.0, 6.0, 7.0) mA cm^{-2} after every five cycles with a fixed Li plating area capacity of 2.5 mAh cm^{-2} , followed by Li stripping until 0.6 V without a time limitation. All cells were tested using multichannel potentiostats (VMP3, BioLogic, France) at 25 °C controlled by a climate chamber (Binder, Germany).

Statistical Analysis: ImageJ software was used to determine the fiber thicknesses and particle sizes. For the determination of the particle sizes, first, a color threshold command was applied for particle selection, followed by a watershed technique to divide extensive and irregular accumulation into separate, circular entities, leading to accurate data retrieval. Manual separation complements the process in cases of massive particle accumulation to ensure conformity with the original images. As STEM-EDS images only provide a small number of particles due to the high magnification, as many pictures as recorded were evaluated to gain the visible statistic in Figure 6c. All analyzed STEM-EDS images can be found in Figure S22, Supporting Information. In addition, particles smaller than 50 nm^2 could not be clearly distinguished from the background and are therefore classified as "dust." Table S3, Supporting Information, includes an overview of the counted number of "dust" at each temperature. Finally, mean values and standard derivations ($\pm\text{SD}$) are calculated with Origin (Originlab Corporation, 2021, USA). The respective sample quantities are listed in the captions of the corresponding figure.

Supporting Information

Supporting Information is available from the Wiley Online Library or from the author.

Acknowledgements

This work was financially supported by the project of "High Performance Solid-State Batteries" (HIPSTER) from "Ministerium für Kultur und Wissenschaft des Landes Nordrhein-Westfalen," and the project of Forschungsinfrastruktur für zukünftige Batteriegenerationen (NextGenBat) from Bundesministerium für Bildung, Wissenschaft, Forschung und Technologie under support number 1703F112. The XPS study in this work was carried out with the support of the Karlsruhe Nano Micro Facility (KNMFi, www.knmf.kit.edu), a Helmholtz Research Infrastructure at Karlsruhe Institute of Technology (KIT). Furthermore, the authors would like to thank Prof. Dr. Josef Granwehr for helpful discussions.

Conflict of Interest

The authors declare no conflict of interest.

Author Contributions

Dana Schmidt: Conceptualization: (lead); Formal analysis: (lead); Investigation: (lead); Methodology: (lead); Visualization: (lead); Writing—original draft: (lead). **Sandro Schöner:** Formal analysis: (supporting); Investigation: (supporting); Methodology: (supporting); Writing—review and editing: (supporting). **Michael K. Steinhoff:** Formal analysis: (supporting); Writing—review and editing: (supporting). **Roland Schierholz:** Formal analysis: (supporting); Investigation: (supporting); Methodology: (supporting); Visualization: (supporting); Writing—review and editing: (supporting). **Kevin Steinhauer:** Formal analysis: (supporting); Investigation: (supporting); Visualization: (supporting). **Davis Thomas Daniel:** Investigation: (supporting); Methodology: (supporting); Visualization: (supporting); Writing—review and editing: (supporting). **Sebastian Speer:** Investigation: (supporting); Writing—review and editing: (supporting). **Ansgar Kretzschmar:** Formal analysis: (supporting); Methodology: (supporting); Writing—review and editing: (supporting). **Fabian Jeschull:** Formal analysis: (supporting); Supervision: (supporting); Writing—review and editing: (supporting). **Anna Windmüller:** Writing—review and editing: (supporting). **Chih-Long Tsai:** Validation: (supporting); Writing—review and editing: (supporting). **Hermann Tempel:** Supervision: (supporting); Writing—review and editing: (supporting). **Shicheng Yu:** Conceptualization: (supporting); Formal analysis: (supporting); Project administration: (lead); Supervision: (lead); Visualization: (supporting); Writing—review and editing: (lead). **Rüdiger-A. Eichel:** Funding acquisition: (lead); Resources: (lead); Supervision: (supporting); Writing—review and editing: (supporting).

Data Availability Statement

The data that support the findings of this study are available in the Supporting Information of this article.

Keywords

3D interlayer, carbonization temperature, current collector modification, Li deposition, lithiophilic–lithiophobic gradient

Received: June 15, 2024

Revised: September 16, 2024

Published online:

- [1] L. Ma, J. Cui, S. Yao, X. Liu, Y. Luo, X. Shen, J.-K. Kim, *Energy Storage Mater.* **2020**, 27, 522.
- [2] K. Lin, X. Qin, M. Liu, X. Xu, G. Liang, J. Wu, F. Kang, G. Chen, B. Li, *Adv. Funct. Mater.* **2019**, 29, 1903229.
- [3] H. Chen, M. Li, C. Li, X. Li, Y. Wu, X. Chen, J. Wu, X. Li, Y. Chen, *Chin. Chem. Lett.* **2022**, 33, 141.
- [4] T.-T. Zuo, X.-W. Wu, C.-P. Yang, Y.-X. Yin, H. Ye, N.-W. Li, Y.-G. Guo, *Adv. Mater.* **2017**, 29.
- [5] F. Cheng, X. Yang, O. Ka, L. Wen, X. Wang, W. Lu, *J. Mater. Chem. A* **2023**, 11, 4205.
- [6] S. Schöner, D. Schmidt, X. Chen, K. Dzieciol, R. Schierholz, P. Cao, A. Ghamlouche, F. Jeschull, A. Windmüller, C.-L. Tsai, X. Liao, H. Kungl, G.-M. Zhong, Y. Chen, H. Tempel, S. Yu, R.-A. Eichel, *ACS Nano* **2024**, 18, 17924.
- [7] C. Liu, Y. Bai, W. Li, F. Yang, G. Zhang, H. Pang, *Angew. Chem. Int. Ed.* **2022**, 61, e202116282.
- [8] S.-H. Wang, Y.-X. Yin, T.-T. Zuo, W. Dong, J.-Y. Li, J.-L. Shi, C.-H. Zhang, N.-W. Li, C.-J. Li, Y.-G. Guo, *Adv. Mater.* **2017**, 29, 1703729.
- [9] L. Liu, Y.-X. Yin, J.-Y. Li, N.-W. Li, X.-X. Zeng, H. Ye, Y.-G. Guo, L.-J. Wan, *Joule* **2017**, 1, 563.
- [10] R. Zhang, X.-B. Cheng, C.-Z. Zhao, H.-J. Peng, J.-L. Shi, J.-Q. Huang, J. Wang, F. Wei, Q. Zhang, *Adv. Mater.* **2016**, 28, 2155.
- [11] C. Chen, J. Guan, N. W. Li, Y. Lu, D. Luan, C. H. Zhang, G. Cheng, L. Yu, X. W. D. Lou, *Adv. Mater.* **2021**, 33, e2100608.
- [12] H. Zhou, G. Zhu, S. Dong, P. Liu, Y. Lu, Z. Zhou, S. Cao, Y. Zhang, H. Pang, *Adv. Mater.* **2023**, 35, e2211523.
- [13] H. Liu, X. Yue, X. Xing, Q. Yan, J. Huang, V. Petrova, H. Zhou, P. Liu, *Energy Storage Mater.* **2019**, 16, 505.
- [14] Y. An, H. Fei, G. Zeng, X. Xu, L. Ci, B. Xi, S. Xiong, J. Feng, Y. Qian, *Nano Energy* **2018**, 47, 503.
- [15] H. Zhou, Y. Sun, H. Yang, Y. Tang, Y. Lu, Z. Zhou, S. Cao, S. Zhang, S. Chen, Y. Zhang, H. Pang, *Adv. Sci.* **2023**, 10, e2303636.
- [16] R. Pathak, K. Chen, F. Wu, A. U. Mane, R. V. Bugga, J. W. Elam, Q. Qiao, Y. Zhou, *Energy Storage Mater.* **2021**, 41, 448.
- [17] R. Zhang, X.-R. Chen, X. Chen, X.-B. Cheng, X.-Q. Zhang, C. Yan, Q. Zhang, *Angew. Chem., Int. Ed.* **2017**, 56, 7764.
- [18] Y.-W. Song, P. Shi, B.-Q. Li, X. Chen, C.-X. Zhao, W.-J. Chen, X.-Q. Zhang, X. Chen, Q. Zhang, *Matter* **2021**, 4, 253.
- [19] B. A. Newcomb, *Composites Part A: Appl. Sci. Manuf.* **2016**, 91, 262.
- [20] M. Inagaki, Y. Yang, F. Kang, *Adv. Mater.* **2012**, 24, 2547.
- [21] B. Zhang, Y. Yu, Z.-L. Xu, S. Abouali, M. Akbari, Y.-B. He, F. Kang, J.-K. Kim, *Adv. Energy Mater.* **2014**, 4, 1301448.
- [22] T.-H. Hsueh, M.-C. Wang, S.-E. Liu, B.-H. Wu, Y.-C. Li, D.-G. Tsai, S.-M. Chang, A. Shiue, K.-Y. Chin, *Electrochem. Commun.* **2023**, 150, 107478.
- [23] Z. Zhang, M. Zhao, M. Xia, R. Qi, M. Liu, J. Nie, Z. L. Wang, X. Lu, *Adv. Funct. Mater.* **2019**, 29, 1806400.
- [24] S.-H. Wang, J. Yue, W. Dong, T.-T. Zuo, J.-Y. Li, X. Liu, X.-D. Zhang, L. Liu, J.-L. Shi, Y.-X. Yin, Y.-G. Guo, *Nat. Commun.* **2019**, 10, 4930.
- [25] H. Zhang, X. Liao, Y. Guan, Y. Xiang, M. Li, W. Zhang, X. Zhu, H. Ming, L. Lu, J. Qiu, Y. Huang, G. Cao, Y. Yang, L. Mai, Y. Zhao, H. Zhang, *Nat. Commun.* **2018**, 9, 3729.
- [26] Y. Zhang, M. Yao, T. Wang, H. Wu, Y. Zhang, *Angew. Chem., Int. Ed.* **2024**, e202403399.
- [27] C. Wang, M. Liu, M. Thijs, F. G. B. Ooms, S. Ganapathy, M. Wagemaker, *Nat. Commun.* **2021**, 12, 6536.
- [28] M. Liu, N. Deng, J. Ju, L. Wang, G. Wang, Y. Ma, W. Kang, J. Yan, *ACS Appl. Mater. Interfaces* **2019**, 11, 17843.
- [29] Z. T. Wondimkun, W. A. Tegegne, J. Shi-Kai, C.-J. Huang, N. A. Sahalie, M. A. Weret, J.-Y. Hsu, P.-L. Hsieh, Y.-S. Huang, S.-H. Wu, W.-N. Su, B. J. Hwang, *Energy Storage Mater.* **2021**, 35, 334.
- [30] S. Niu, S.-W. Zhang, D. Li, X. Wang, X. Chen, R. Shi, N. Shen, M. Jin, X. Zhang, Q. Lian, R. Huang, A. Amini, Y. Zhao, C. Cheng, *Chem. Eng. J.* **2022**, 429, 132156.
- [31] T. Lavanya, S. Ramaprabhu, *Mater. Res. Express* **2019**, 6, 105005.
- [32] P. Sharrock, M. Melnik, *Can. J. Chem.* **1985**, 63, 52.
- [33] K. B. B. Bleaney, *Proc. R. Soc. Lond. A* **1952**, 214, 451.
- [34] S. I. Al-Resayes, M. Shakir, A. Abbasi, K. M. Y. Amin, A. Lateef, *Spectrochim. Acta A Mol. Biomol. Spectrosc.* **2012**, 93, 86.
- [35] S. A. A. Mansour, *J. Therm. Anal.* **1996**, 46, 263.
- [36] M. Jing, C. Wang, Q. Wang, Y. Bai, B. Zhu, *Polym. Degrad. Stab.* **2007**, 92, 1737.
- [37] C. E. Tait, A. Reckwitz, M. Arvind, D. Neher, R. Bittl, J. Behrends, *Phys. Chem. Chem. Phys.* **2021**, 23, 13827.
- [38] R. S. Havigh, H. M. Chenari, *Sci. Rep.* **2022**, 12, 10704.
- [39] Z. E. Brubaker, J. J. Langford, R. J. Kapsimalis, J. L. Niedziela, *J. Mater. Sci.* **2021**, 56, 15087.
- [40] A. Sadezky, H. Muckenhuber, H. Grothe, R. Niessner, U. Pöschl, *Carbon* **2005**, 43, 1731.
- [41] Y. Wang, D. C. Alsmeyer, R. L. McCreery, *Chem. Mater.* **1990**, 2, 557.
- [42] S. Claramunt, A. Varea, D. López-Díaz, M. M. Velázquez, A. Cornet, A. Cirera, *J. Phys. Chem. C* **2015**, 119, 10123.

- [43] P. A. Goodman, H. Li, Y. Gao, Y. F. Lu, J. D. Stenger-Smith, J. Redepenning, *Carbon* **2013**, *55*, 291.
- [44] C. Marino, J. Cabanero, M. Povia, C. Villevieille, *J. Electrochem. Soc.* **2018**, *165*, A1400.
- [45] L. G. Bulusheva, A. V. Okotrub, A. G. Kurenya, H. Zhang, H. Zhang, X. Chen, H. Song, *Carbon* **2011**, *49*, 4013.
- [46] T.-Z. Hou, X. Chen, H.-J. Peng, J.-Q. Huang, B.-Q. Li, Q. Zhang, B. Li, *Small* **2016**, *12*, 3283.
- [47] L. D. Cremar, B. Jones, N. Martinez, G. Mejia, H. Cortez, E. Muñoz, R. Nava, K. Lozano, *J. Adv. Nanomater.* **2017**, *2*, <https://dx.doi.org/10.22606/jan.2017.24002>.
- [48] M. Ayiania, M. Smith, A. J. Hensley, L. Scudiero, J.-S. McEwen, M. Garcia-Perez, *Carbon* **2020**, *162*, 528.
- [49] Z. Mo, H. Liu, R. Hu, H. Gou, Z. Li, R. Guo, *Ionics* **2018**, *24*, 1505.
- [50] T. Kondo, D. Guo, T. Shikano, T. Suzuki, M. Sakurai, S. Okada, J. Nakamura, *Sci. Rep.* **2015**, *5*, 16412.
- [51] M. Thommes, K. Kaneko, A. V. Neimark, J. P. Olivier, F. Rodriguez-Reinoso, J. Rouquerol, K. S. Sing, *Pure Appl. Chem.* **2015**, *87*, 1051.
- [52] K. A. Cychoz, M. Thommes, *Engineering* **2018**, *4*, 559.
- [53] A. Kretzschmar, V. Selmert, H. Weinrich, H. Kungl, H. Tempel, R.-A. Eichel, *ChemSusChem* **2020**, *13*, 3180.
- [54] J.-H. Park, K. Natesan, *Oxid Met* **1993**, *39*, 411.
- [55] S. Kim, G. Yoon, S.-K. Jung, S. Park, J.-S. Kim, K. Yoon, S. Lee, K. Kang, *ACS Energy Lett.* **2023**, *8*, 9.
- [56] R. Schierholz, D. Kröger, H. Weinrich, M. Gehring, H. Tempel, H. Kungl, J. Mayer, R.-A. Eichel, *RSC Adv.* **2019**, *9*, 6267.
- [57] U. Kurtan, H. Aydin, *J. Energy Storage* **2021**, *42*, 103016.
- [58] W. Ali, V. Shabani, M. Linke, S. Sayin, B. Gebert, S. Altinpinar, M. Hildebrandt, J. S. Gutmann, T. Mayer-Gall, *RSC Adv.* **2019**, *9*, 4553.
- [59] D. He, B. Hu, Q.-F. Yao, K. Wang, S.-H. Yu, *ACS Nano* **2009**, *3*, 3993.
- [60] A. Kawecki, T. Knych, E. Sieja-Smaga, A. Mamala, P. Kwaśniewski, G. Kiesiewicz, B. Smyrak, A. Pacewicz, *Arch. Metall. Mater.* **2012**, *57*, 1261.
- [61] H. J. Sand, *Lond. Edinb. Dubl. Philos. Mag.* **1901**, *1*, 45.
- [62] B. D. Adams, J. Zheng, X. Ren, W. Xu, J.-G. Zhang, *Adv. Energy Mater.* **2018**, *8*, 1702097.
- [63] T. J. Davies, R. R. Moore, C. E. Banks, R. G. Compton, *J. Electroanal. Chem.* **2004**, *574*, 123.
- [64] Z. Liu, J. Du, H. Jia, W. Wang, M. Zhang, T. Li, Y. Nie, T. Liu, K. Song, *Ionics* **2022**, *28*, 3709.
- [65] S. Zheng, Y. Sun, H. Xue, P. Braunstein, W. Huang, H. Pang, *Natl. Sci. Rev.* **2022**, *9*, nwab197.
- [66] A. Khort, S. Roslyakov, P. Loginov, *Nano-Struct. Nano-Obj.* **2021**, *26*, 100727.
- [67] S. S. A. K, A. Dzubinska, M. Reiffers, N. R, *Phys. B: Condens. Matter* **2019**, *575*, 411679.
- [68] A. Kovács, R. Schierholz, K. Tillmann, *JLSRF* **2016**, *2*, A43.
- [69] M. Yamashita, M. Agu, *J. Appl. Phys.* **1984**, *23*, 1499.